




Comparison Between Ground, Helicopter, and Unmanned Aircraft System Magnetic Datasets: A Case Study from the Abitibi Greenstone Belt, Canada

MICHAEL CUNNINGHAM,¹  CLAIRE SAMSON,¹ JEREMY LALIBERTÉ,² MARK GOLDIE,³ ALAN WOOD,⁴
and DAVID BIRKETT⁴

Abstract—This paper presents a direct platform-to-platform comparison of ground, helicopter, and unmanned aircraft system (UAS) magnetic data acquired over a 4.96 km² prospective gold area in the Abitibi Greenstone Belt of the Canadian Precambrian Shield. Qualitative comparison focused on visual inspection of residual and gradient magnetic maps, focusing mainly on features associated with iron formations. Quantitative comparison employed maps of cell-by-cell absolute difference, percent difference, and coherence, as well as three global image similarity parameters: the structural similarity index, the mean squared error, and the peak signal-to-noise ratio. The qualitative comparison revealed that lateral continuity along the dominant E–W structural geological trend was better captured in the ground and UAS data than in the helicopter data. The UAS data had the additional advantage over the ground data of having undergone minimal processing. The quantitative comparison metrics were the same between all three datasets. This study showed that UAS technology is delivering the same data quality as traditional survey techniques in addition being an attractive economic and safety choice.

Keywords: Unmanned vehicle system, magnetics, airborne surveying, mineral exploration.

1. Introduction

Magnetic surveying is a classic survey technique in mineral exploration used to delineate structural features and trends by mapping the spatial distribution of magnetically susceptible rocks in prospective environments. Magnetic exploration surveys are

performed over a wide range of scales, from medium/large-scale (typically up to ≈ 150 km²) to small-scale (≈ 10 km²). Large-scale surveys are usually flown using helicopter or fixed-wing aircraft to cover large territories at reasonable cost (helicopter-borne aeromagnetic surveys in North American currently range between \$35/line-km to over \$100/line-km depending on survey size) albeit at lower resolution. Small-scale helicopter and ground surveys are executed to provide high-resolution data for focussed regions. Surveys using unmanned aircraft systems (UAS) are increasingly being used to bridge the gap between large- and small-scale surveys and have been suggested as replacement or complement to ground surveys. UAS are known for their versatility: they can be launched in nearly all locales, fly in terrains with rough topography, have lower weight and higher manoeuvrability, and are safer to personnel. UAS operations are often subject to location-specific regulations and flight operation approvals processes, however, these are less complex and associated costs are similar or less than for traditional platforms.

Fixed-wing (Cherkasov et al., 2016; Funaki et al., 2014; Wood et al., 2016; Zhang et al., 2011) or rotary-wing (Bian et al., 2021; Cunningham et al., 2018, 2021; de Smet et al., 2021; Le Maire et al., 2020; Malehmir et al., 2017; Parshin et al., 2018; Parvar et al., 2018; Sterligov et al., 2018; Stoll, 2013; Tuck et al., 2019; Walter et al., 2019a) UAS can carry magnetic sensors. Presently, most research efforts focus on rotary-wing UAS due their smaller size (and therefore less stringent regulations) and reduced take-off and landing constraints. Payloads onboard UAS consist of either total magnetic intensity (TMI) or fluxgate sensors, that are mounted rigidly

¹ Department of Earth Sciences, Carleton University, Ottawa, ON, Canada. E-mail: Michael.Cunningham@carleton.ca

² Department of Mechanical and Aerospace Engineering, Carleton University, Ottawa, ON, Canada.

³ IAMGOLD Corporation, 401 Bay St #3200, Toronto, ON M5H 2Y4, Canada.

⁴ Stratus Aeronautics, #123, 3191 Thunderbird Crescent, Burnaby, BC V5A 3G1, Canada.

(Cunningham et al., 2018; Eck & Imbach, 2011; Stoll, 2013; Tuck et al., 2019; Wood et al., 2016) or are suspended beneath the platform (Malehmir et al., 2017; Parshin et al., 2018; Parvar et al., 2018; Sterligov et al., 2018; Walter et al., 2019a, 2019b).

Only a few studies comparing magnetic data from UAS and traditional platforms have been published (Cunningham et al., 2018; Walter et al., 2019c). The purpose of this paper is to provide detailed qualitative and quantitative comparisons between three different datasets—ground, helicopter, and UAS—over the same location in the Abitibi Greenstone Belt of the Canadian Precambrian Shield. These comparisons are aimed at unraveling the differences between each platform and, more specifically, at highlighting the merits of UAS surveying for targeted mineral exploration.

2. Comparison Study Area

The comparison study area is part of the Nelligan property (Fig. 1), which is owned by IAMGOLD Corporation and Vanstar Mining Resources. The property is located in the Province of Quebec, approximately 35 km south-east of Chapais and 55 km south-west of Chibougamau (a regional geological map detailing rock types, structures, and mineral ore zones is presented in Fig. 2). It lies within the Caopatina-Desmaraisville volcano-sedimentary segment of the Abitibi Greenstone Belt of the Archean Superior Province of the Canadian Precambrian Shield. The Caopatina-Desmaraisville segment is primarily composed of the Deloro Assemblage (2734–2724 Ma) and shows evidence of multiple volcanic cycles. Pre-deformational regional folds (orientated N–S to NNW–SSE) are preserved and related to the Kenorean Orogeny (Carrier et al., 2019) which also caused regional schistosity (Guha et al., 1991). Following this orogeny, the primary deformational event is a N–S shortening producing E–W tectonic fabric and a deformation corridor indicated by longitudinal faulting (Carrier et al., 2019). The Druillettes Syncline and two groups of faults (E–W and SE–NW trending) are associated with this shortening event (Guha et al., 1991) (Fig. 1). Two younger fault groups are also observed;

Figure 1

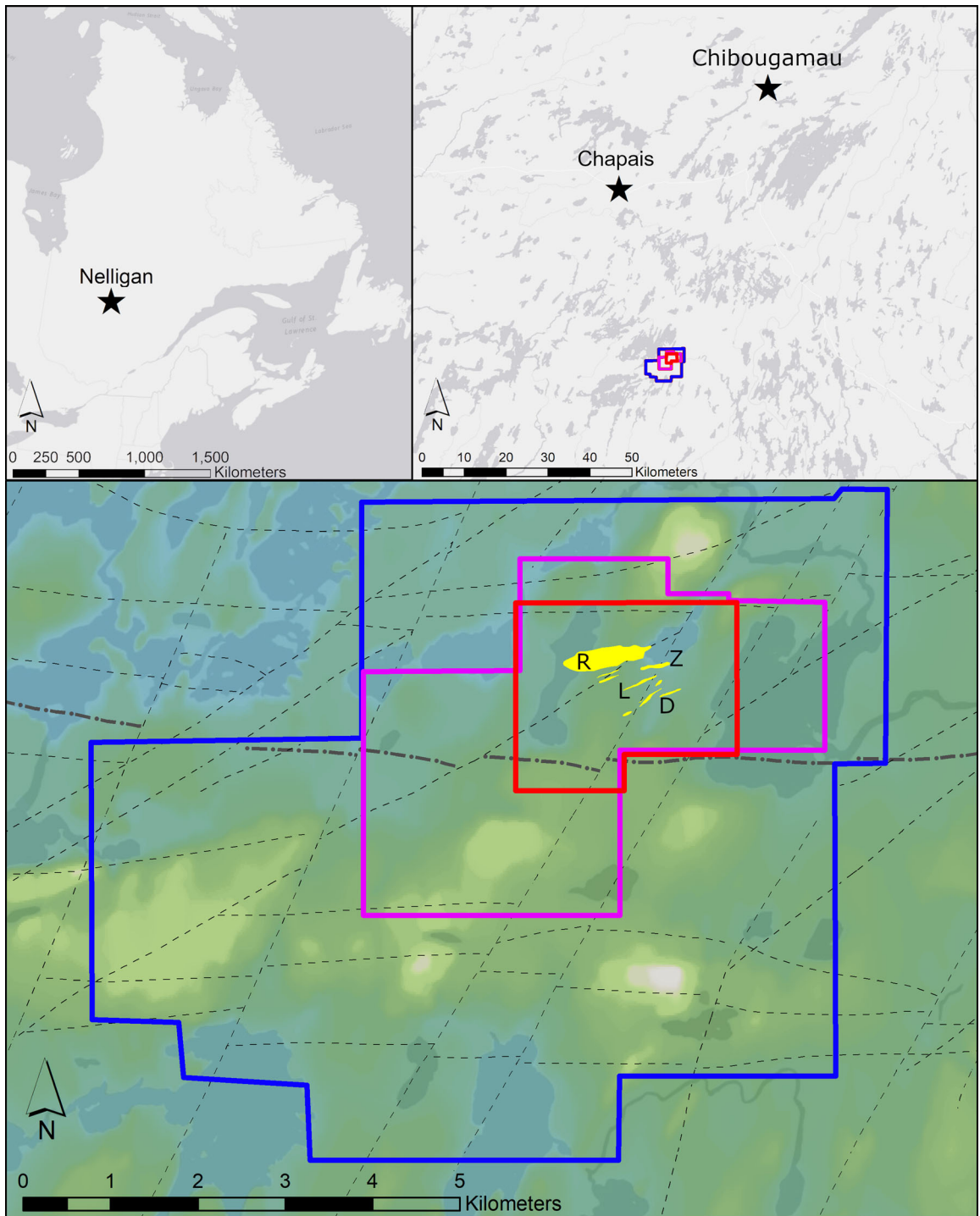
Location maps. Top left: Eastern Canada; top right: central Quebec; and bottom: three aeromagnetic survey areas. Gold zones overlain on elevation in yellow: R—Renard; Z—Zone 36; L—Liam; and D—Dan. Elevation data from Government of Canada (2017)




a NE–SW trending group cutting regional schistosity and a NNE–SSW group associated with the Grenville Orogeny. The north and south limbs of the Druillettes syncline are subvertical, striking approximately east–west and dipping 80° on average. Metasediments of the Caopatina formation are found within the center of the syncline, and primarily consists of metamorphosed units with protoliths of feldspathic wackes, siltstones-mudstones-argillites, greywackes, conglomerates, and layers of iron formation. On either side of the syncline (northward and southward) are metavolcanics and metasediments which primarily consist of basalts and gabbros of tholeiitic composition.

Three separate magnetic surveys were performed over the Nelligan property—ground, helicopter, and UAS (Fig. 1, Table 1). The 4.96 km² UAS survey area was selected as the comparison study area. The comparison study area is generally flat with some rolling hills (≤ 30 m elevation change). There are thick glacial deposits within the area, which is covered by the boreal forest, and no known outcrop.


The comparison study area features four different gold mineralization zones (Renard, Zone 36, Liam, and Dan) (Fig. 1). The mineralization zones are hosted in metasedimentary rocks of the Deloro assemblage, which is atypical of gold mineralization for Abitibi type deposits (typically gold mineralization is hosted in the metavolcanic rocks). They are generally located at the boundary between upper greenschist and amphibolite facies, and are adjacent to first-order crustal faults.

Previous magnetic surveys have been performed over the Nelligan property to map and delineate structural trends. Along with past drilling projects, these surveys have identified local iron formations (IF) as the sources of the strongest magnetic responses in the area. The IF layers have been used to develop the property's structural framework (Carrier et al., 2019). Inversion of the UAS aeromagnetic data



-  UAS Survey and Comparison Study Area
-  Ground Survey Area
-  Helicopter Survey Area

-  Gold Zones
-  Faults
-  Druillettes Syncline Axis

Elevation (ASL) (m)
High : 546

Low : 355

produced models that are consistent with the presence of near-vertical structures or thin sheets steeply dipping towards the north and south (Cunningham et al., 2021), further supporting this interpretation.

3. Magnetic Survey Descriptions

3.1. Ground Survey

The ground TMI survey was conducted between July and August 2013. This survey employed a GEM GSM-19 proton precession Overhauser magnetometer and covered an area of 14.11 km² and 95.7 line-km. Traverse lines were oriented in a N-S direction with a line spacing of 100 m. TMI data was recorded at station intervals of 12.5 m. Approximately 46.5 line-km were completed within the comparison study area at 2 m above ground level (AGL) (Fig. 3—left).

3.2. Helicopter Survey

The helicopter TMI survey was conducted between 8 July 2015 to 10 July 2015. This survey was a combined time-domain electromagnetic and

magnetic survey. The helicopter was instrumented with two caesium vapour sensors (spaced 12.5 m apart) allowing for TMI and cross-line gradient surveying. An area of 52.70 km² was covered at a nominal altitude of 50 m AGL by draping topography, corresponding to 587.7 line-km. Traverse lines were oriented in a N-S direction with a line spacing of 100 m and tie lines were spaced at 1000 m intervals. TMI data from each sensor was recorded at a sampling frequency of 10 Hz and compensated for aircraft attitude. A total of 51.6 line-km (46.5 traverse line-km and 5.1 tie line-km) were completed within the comparison study area (Fig. 3—middle).

3.3. UAS Survey

Between September 29, 2018 to October 3, 2018, Stratus Aeronautics flew a UAS survey with the prototype SkyLance 6200 hexacopter (Fig. 4). A total of area of 4.96 km² was covered, corresponding to 319.7 line-km, by holding a constant altitude above sea level, corresponding approximately to 50 m AGL. A subset of 129.1 line-km (97.4 traverse line-km and 31.7 tie line-km) are considered in the present

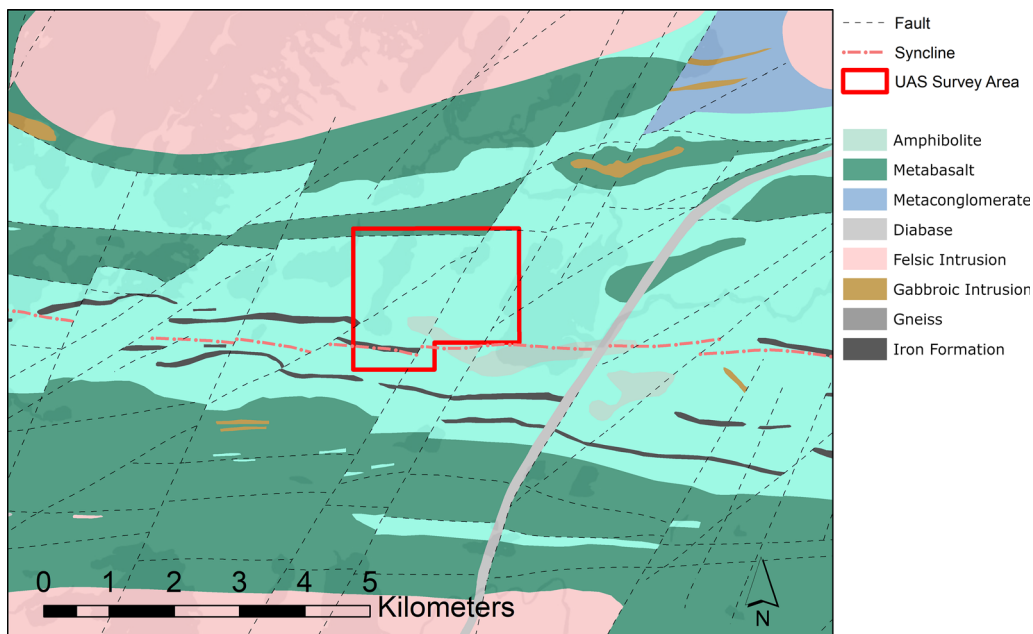


Figure 2
Geological map of the Nelligan survey area

Table 1
Magnetic survey parameters

| System | Ground | Helicopter | UAS |
|-------------------------|--|--------------------------------|-------------------------------------|
| Line-km (km) | 95.7 | 587.7 | 319.7 |
| Line spacing (m) | 100 | Traverse: 100 Tie: 1000 | Traverse: 50 and 25 Tie: 150 |
| Average speed (km/h) | 4.5 | 80 | 30 |
| Altitude (AGL) (m) | 2 | 50 | 50 |
| Line Azimuth (°) | 0/180 | Traverse: 0/180 Tie: 90/270 | Traverse: 0/180 Tie: 90/270 |
| Sensor | GEM GSM-19 Proton Precession Overhauser | Geometrics Caesium Vapour | Geometrics G-823A Caesium Vapour |
| Sampling frequency (Hz) | 1 | 10 | 10 |
| Spatial sampling (m) | 12.5 | 2.2 | 0.8 |
| Time to complete survey | 1 month | 3 days | 3 days |

study (Fig. 3—right). Traverse lines were oriented in a N–S direction with a traverse and tie line spacing of 50 m and 150 m, respectively. Uncompensated TMI data was recorded at a sampling frequency of 10 Hz. A repeatability test executed along a N–S oriented line showed that the UAS was very stable in flight with average standard deviations from nominal altitude and easting being 1.8 m and 0.7 m, respectively (Cunningham et al., 2021).

The SkyLance 6200 hexacopter employs an autopilot that is capable of automatic take-off and landing, as well as following predetermined waypoints. The platform weighs approximately 15 kg excluding the payload. It carries a payload weighing approximately 5 kg primarily consisting of a Geometrics G-823A caesium vapour magnetometer. The

UAS has a flight endurance of approximately 30 min and can fly at an average of 32 km/h ground speed. Typically, 3 people are required on the ground for UAS survey operations.

4. Results

4.1. Residual Magnetic Intensity and Gradients

Processing of each dataset followed a typical workflow, using Seequent's (formerly Geosoft) Oasis Montaj processing software, and included: diurnal correction, lag corrections, line levelling, and interpolation. Diurnal corrections were performed by subtraction of base station data. Base station data

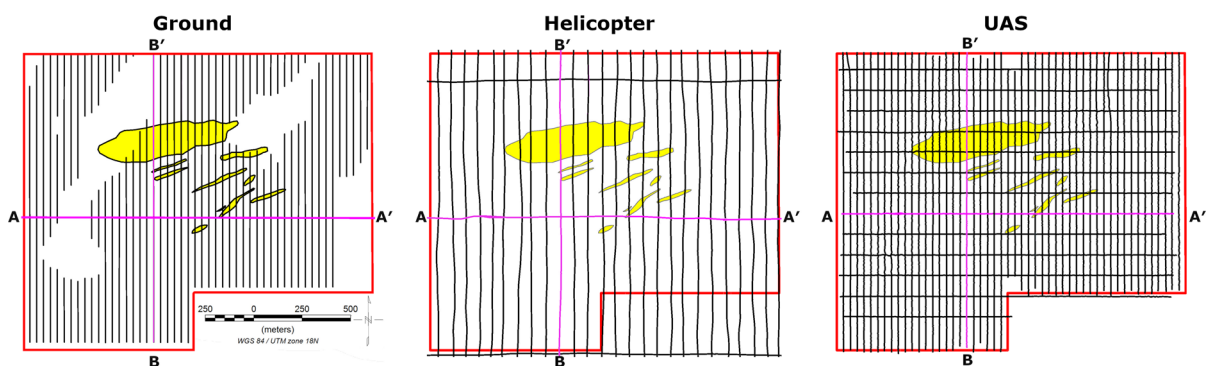


Figure 3

Survey line paths for each survey platform with the comparison survey area is outlined in red and gold ore zones are highlighted in yellow. Left—2013 ground magnetic survey. Middle—2015 helicopter survey. Right—2018 UAS survey. Magenta lines, labelled A–A' and B–B', highlight the profiles presented in Fig. 5



Figure 4

Stratus Aeronautics SkyLance 6200 with front-mounted caesium vapour magnetometer

was collected at a sampling frequency of 1 Hz. A moving average with a 60 s window was applied and the data was linearly interpolated to a frequency of 10 Hz. The interpolated data was then subtracted from the raw magnetic data collected by each survey platform. Further lag corrections and line levelling was applied to the helicopter and UAS datasets. Lag corrections apply a temporal or positional shift in the datasets to account for the positional offset between the positional sensor and the magnetic sensor. Line levelling redistributes corrugations within parallel traverse lines to reduce line-by-line errors by using intersection points between traverse and tie lines. Minimum curvature interpolation at $\frac{1}{4}$ the flight line spacing was then applied, following standard industry practice (Lee & Morris, 2013), to produce magnetic maps of cell size 25 m \times 25 m (note that interpolation of the UAS data was performed at $\frac{1}{2}$ of the flight line spacing to match the spatial resolution of ground and helicopter data). In-line, cross-line, and vertical gradients were calculated from the residual magnetic intensity (RMI) data.

Magnetic intensity profiles along two lines highlighted in Fig. 3, are shown in Fig. 5. Profile A–A', oriented west to east and crossing Feature 3 described below, shows less intensity variations since it is parallel to structural trends. Profile B–B', oriented south or north and intersecting perpendicularly features 1, 3, and 4 described below, exhibit larger intensity variations. Overall, Fig. 5 shows that the magnetic profiles for the 3 datasets from a 50 m altitude (either calculated or directly recorded) match closely.

Figures 6, 7, 8, and 9 show the original ground data, the ground data upward continued (UC) to 50 m above ground level (AGL), the helicopter data, and the UAS data, respectively.

The magnetic intensity maps from each survey (Figs. 6, 7, 8, and 9 (top left)) reveal a structurally complex region exhibiting several known and inferred IF units. Feature 1 is located along the northern edge of the comparison study area and might correspond to two parallel E–W trending IF units. Feature 2 is interpreted as a continuation of Feature 1 but was displaced by a series of faults (striking SW–

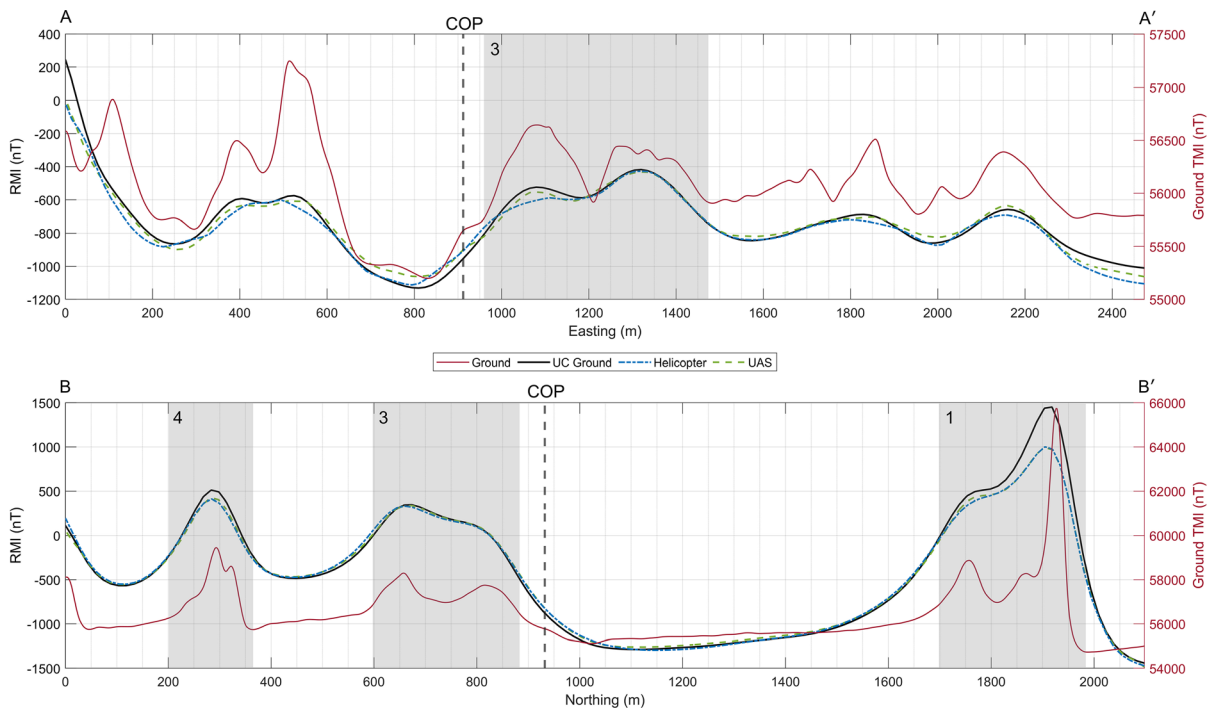


Figure 5

Profile plots of residual magnetic intensity from each survey dataset along two survey lines that are highlighted in Fig. 4. A–A' is a tie line, from west to east across the center of the survey area. B–B' is a traverse line from south to north. The crossover point (COP) between the two lines is marked by a dashed vertical line. Key features are numbered according to the regions marked in Figs. 6, 7, 8, 9, and 10 and their extents are highlighted in grey

NE and E–W) causing an offset between the features. Feature 3, located in the center of the comparison survey area, follows the same local (SW–NE) fault. This region is where the Liam and Dan gold mineralization zones are located. Feature 4 is an E–W trending IF and coincides with the axis of the Druillettes Syncline. It is the only IF in the comparison study area that is featured on regional geological maps (Carrier et al., 2019 and SIGEOM, 2020). The northern segment of Feature 4 appears as though it may have been displaced from the southern segment through secondary faulting or folding.

To allow a direct comparison between the three magnetic datasets, the ground data was upward continued to 50 m AGL which is the nominal altitude of the helicopter and UAS surveys. The original ground data (Fig. 6) has captured fine structural details, especially within the IF units, but does exhibit artifacts presumably due to uneven spacing coverage. These artifacts are particularly prominent in the

gradient maps. Applying upward continuation to the data (Fig. 7) gives a smoother appearance to the data but some details are lost. Feature 2, for example, appears as three distinct parallel structures truncated by a NE–SW fault to the west in the original ground data, but only appear as two faint parallel E–W trending structures in the upward continued ground data.

Visually comparing the upward continued ground, helicopter, and UAS RMI maps (Figs. 7, 8, 9 (top left)) reveals some notable differences in terms of amplitude and lateral continuity. The amplitude of the magnetic anomalies associated with the four key features described above are strongest in the upward continued ground data. Lateral continuity along the dominant E–W structural trend is better expressed in the upward continued ground and UAS data than in the helicopter data. In the case of the upward continued ground data, however, continuity might be a product of mathematical operations. On the other

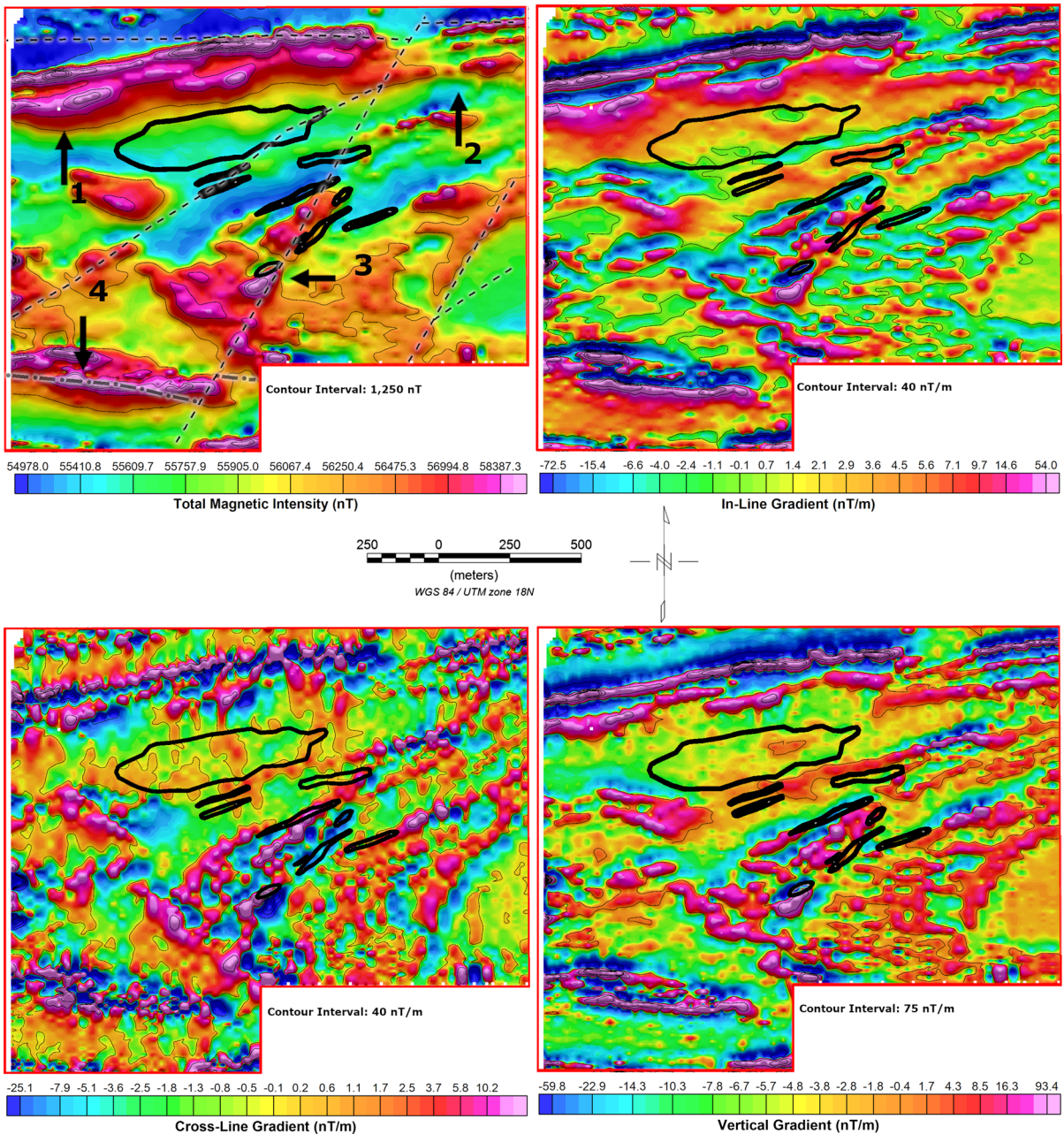


Figure 6

Ground magnetic maps of the comparison survey area. Black lines delineate the gold zones. Dashed lines are local faults. Dash-dot lines are folds (syncline). Arrows point to the key features described in Sect. 4.1

hand, the continuity of the UAS data can be interpreted as a genuine geological signature since the data has undergone minimal processing. The helicopter data suffers from resolution effects due to the large traverse line spacing used during data

acquisition [25–50 m for the UAS data versus 100 m for the helicopter data (Table 1)]. Consequently, it did not capture details of the internal structure of Features 1 and 4 as well as the upward continued ground data and the UAS data.

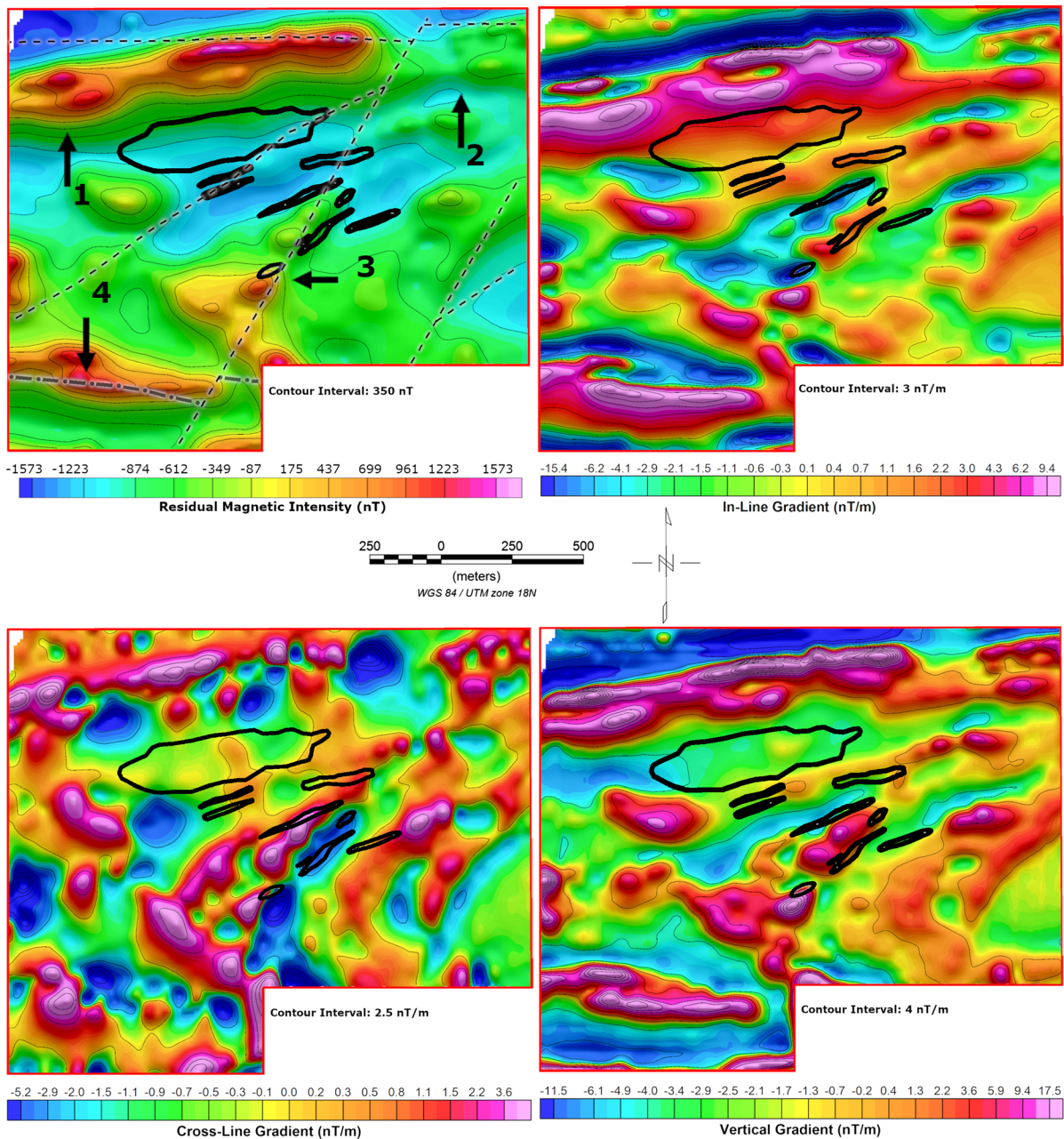


Figure 7

Upward continued to 50 m AGL ground RMI maps of the comparison survey area. Black lines delineate the gold zones. Dashed lines are local faults. Dash-dot lines are folds (syncline). Arrows point to the key features described in Sect. 4.1

In-line, cross-line and vertical gradient maps (Figs. 7, 8, and 9 (top right, bottom left, bottom right)) highlight the structural boundaries between the key features and surrounding geology. The four features discussed above can be easily identified in the in-line and vertical gradient maps and, to a lesser

extent, on the cross-line gradient map. The cross-line gradient maps tend to be lesser quality due to presence of resolution artifacts associated with interpolation effects for the upward continued ground data and to lower spatial sampling in the E-W direction (traverse lines) for the helicopter and UAS datasets.

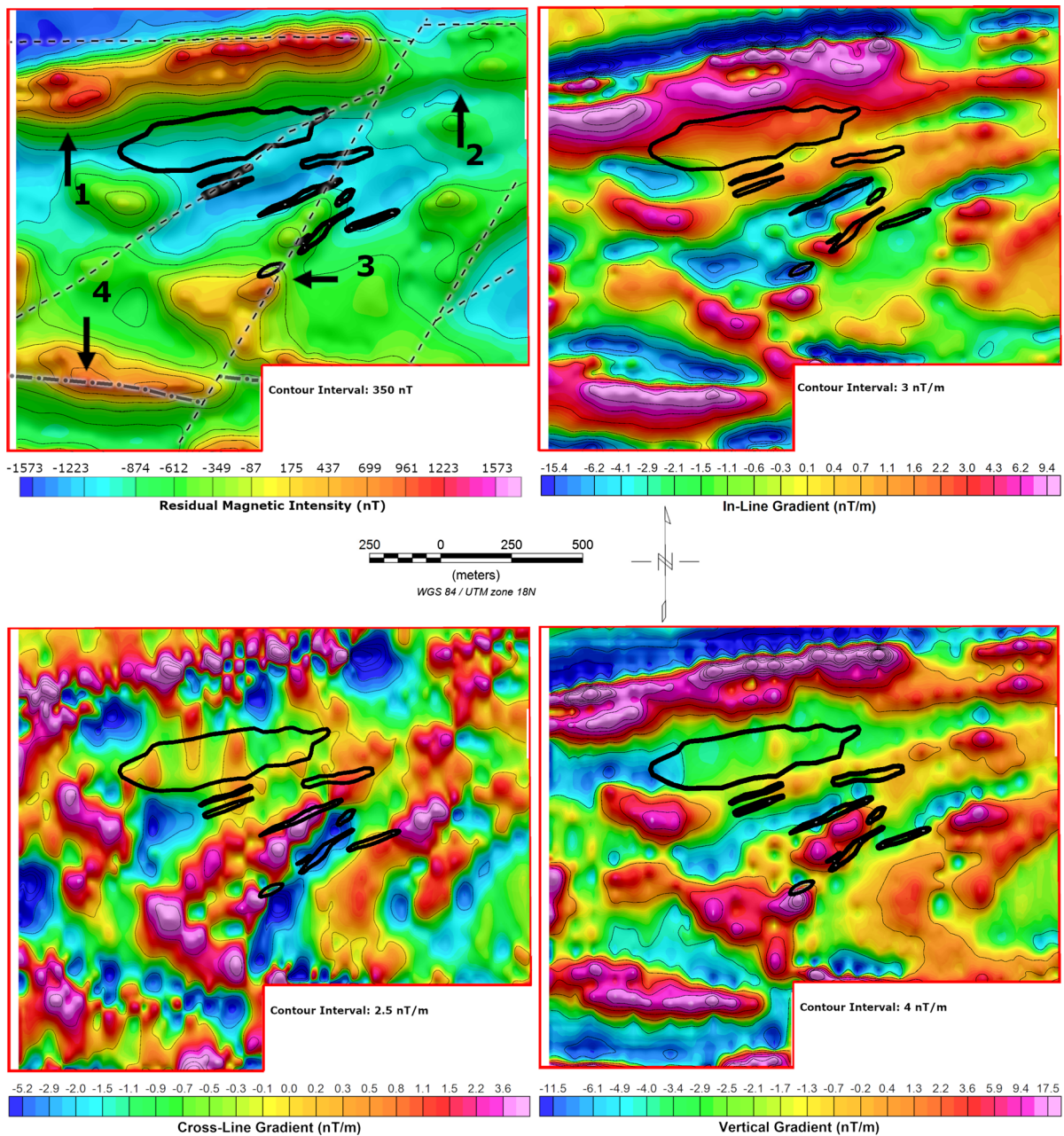


Figure 8

Helicopter RMI maps of the comparison survey area. Black lines delineate the gold zones. Dashed lines are local faults. Dash-dot lines are folds (syncline). Arrows point to the key features described in Sect. 4.1

4.2. Quantitative Dataset Comparison

Two metrics assessing the differences between each dataset were employed. First, the absolute difference between each dataset was calculated on a grid cell by grid cell basis. Second, the percent difference between each normalized dataset on a grid

cell by grid cell basis was determined, where the percent difference is calculated as the difference between two datasets in each grid cell divided by the average value in that grid cell.

The first metric provides a direct measure of the differences between each dataset whereas the second

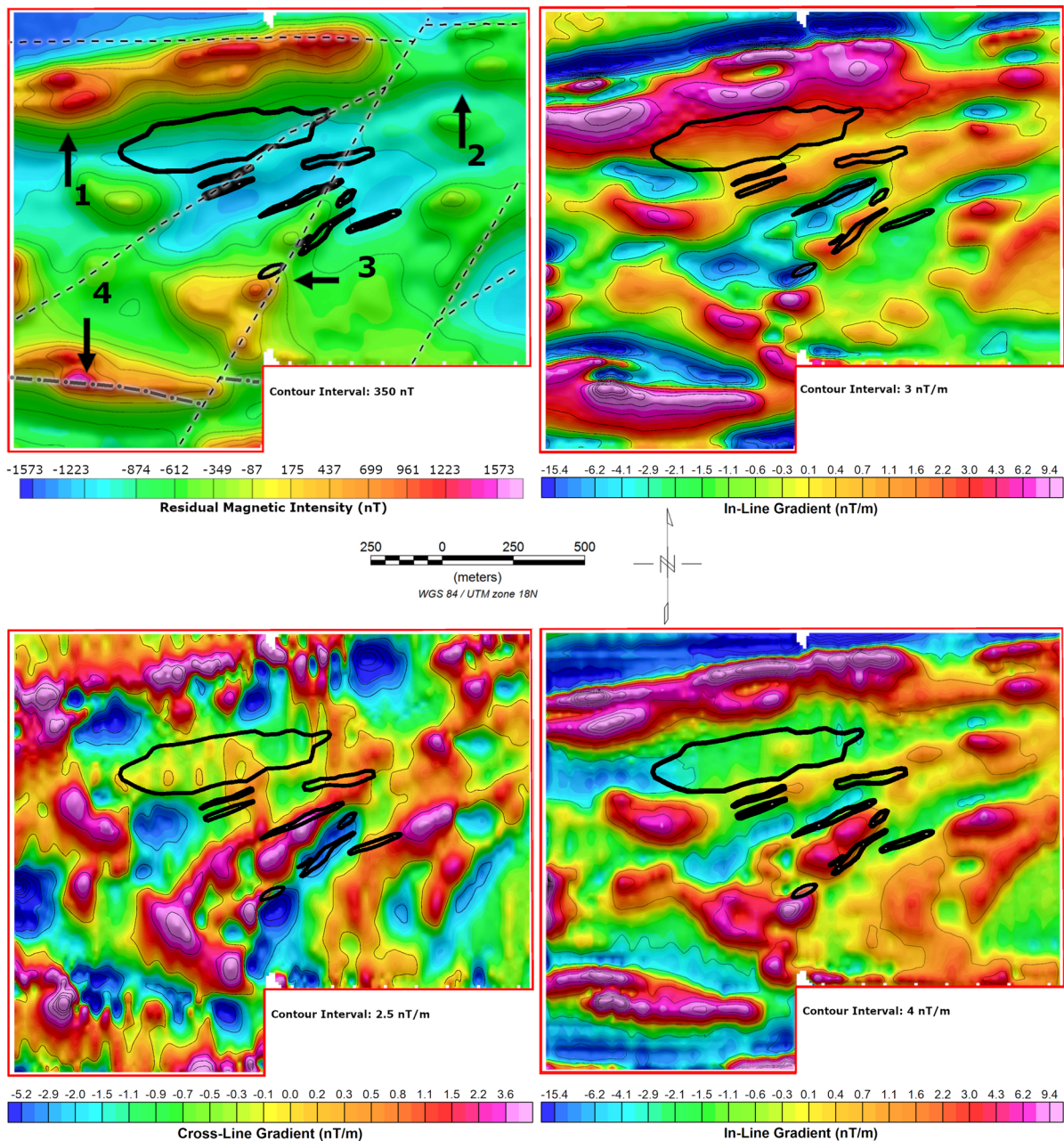


Figure 9

UAS RMI maps of the comparison survey area. Black lines delineate the gold zones. Dashed lines are local faults. Dash-dot lines are folds (syncline). Arrows point to the key features described in Sect. 4.1

method provides a normalized comparison. The first method highlights regions where there is more difference but ignores the possibility that this could be due to the fact that the magnetic intensity might be stronger locally. The percent difference reduces the effects of local variations in magnetic intensity.

Figure 10 presents the absolute (left) and percent differences (middle) between the UAS and helicopter datasets (top), UC ground and UAS datasets (middle), and UC ground and helicopter (bottom) datasets, respectively. Higher absolute differences are primarily situated over higher gradient regions (Features 1,

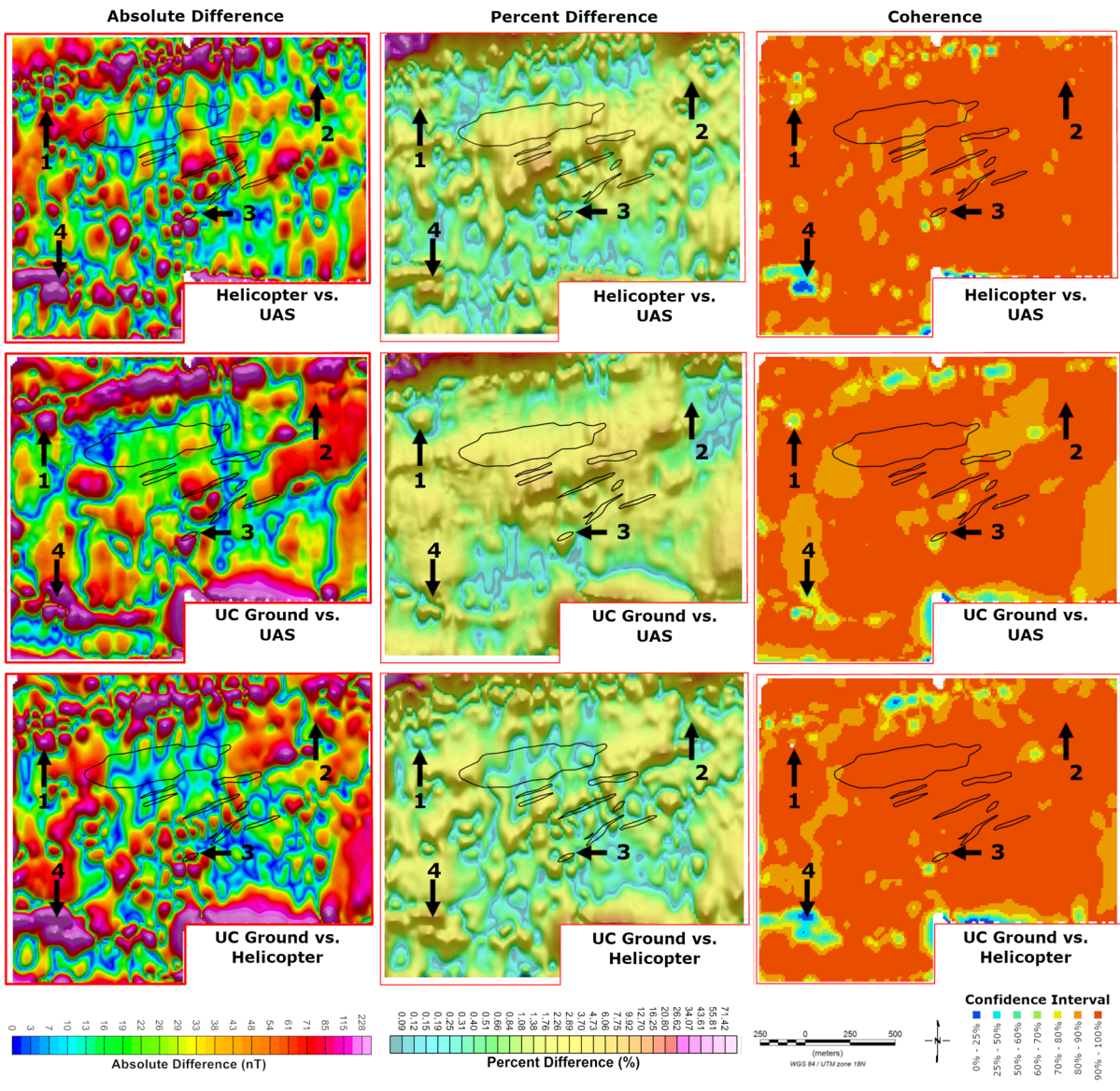


Figure 10

Left—absolute differences between the three datasets. Middle—percent difference between the three datasets. Right—level of confidence in coherence between the three datasets. Black lines delineate the gold zones. Labelled black arrows point to the key features described in Sect. 4.1

3, and 4) surrounding the IF units. This is probably the consequence of small variations in altitude and/or positioning between the platforms, an effect that is exacerbated in high gradient regions. Percent difference does not emphasise the regions of higher gradient to the same extent. Higher percent differences are found in the center of the survey area and mainly associated with the UAS dataset. This is likely

because the UAS was held a constant altitude with respect to sea level (no draping), whereas both the helicopter and ground are effectively following topography; the center is lower in elevation than the edges of the survey area (Fig. 1).

A statistical test was also performed to determine the coherence between each dataset (Sampietro et al., 2013). Assuming each survey provides independent

maps, m_j , m_k , of the local magnetic field, T , where j and k correspond to the two datasets being compared, we have for each grid cell, i :

$$\Delta T_i^{m_j, m_k} = T_i^{m_j} - T_i^{m_k} = 0,$$

with the variance σ^2 given by:

$$\sigma^2(\Delta T_i^{m_j, m_k}) = \sigma^2(T_i^{m_j}) + \sigma^2(T_i^{m_k}).$$

Statistical interference can be used to test that the hypothesis that:

$$\Delta T_i^{m_j, m_k} = 0,$$

is true for multiple confidence intervals. The resultant coherence maps, for multiple confidence intervals, are presented in Fig. 10 (right) and summarized in Table 2. For each comparison set, over 93% of the survey area shows coherence within or higher than the 80–90% confidence interval. However, regions of lower coherence are observed for all three platforms near the key features previously identified. Feature 4 has the lowest coherence in all three comparisons and low coherence is also observed along the eastern flank of Feature 1.

A series of additional quantitative comparison metrics were also employed: (1) the structural similarity index (SSIM); the mean squared error (MSE); and the peak signal-to-noise ratio (PSNR). Each metric was computed from normalized datasets so that they range between 0 and 1.

The SSIM is a strategy used in image analysis to measure the similarity between two images (Wang et al. 2004); a SSIM value of 0 means there is no similarity between the images, and a value of 1 means the images are identical.

Table 2

Coherence of grid cells for each confidence interval as well as the cumulative total within that interval and higher

| Confidence interval (%) | UAS vs. helicopter (%) | UAS vs. UC ground (%) | UC ground vs. helicopter (%) |
|-------------------------|------------------------|-----------------------|------------------------------|
| 0–25 | 0.21 | 0.04 | 0.22 |
| 25–50 | 0.41 | 0.26 | 0.71 |
| 50–60 | 0.41 | 0.54 | 0.83 |
| 60–70 | 0.61 | 1.31 | 1.46 |
| 70–80 | 1.74 | 3.10 | 2.92 |
| 80–90 | 11.66 | 23.71 | 15.76 |
| 90–100 | 84.95 | 71.02 | 78.08 |

$$SSIM(x, y) = [l(x, y)]^\alpha \cdot [c(x, y)]^\beta \cdot [s(x, y)]^\gamma,$$

with

$$l(x, y) = \frac{2\mu_x\mu_y + C_1}{\mu_x^2 + \mu_y^2 + C_1},$$

$$c(x, y) = \frac{2\sigma_x\sigma_y + C_2}{\sigma_x^2 + \sigma_y^2 + C_2},$$

$$s(x, y) = \frac{\sigma_{xy} + C_3}{\sigma_x\sigma_y + C_3},$$

where μ_x, μ_y , σ_x , σ_y , and σ_{xy} are local means, standard deviation, and cross-variance for images x and y . C_1 , C_2 , and C_3 are constants that are included to avoid instability when μ_x and μ_y and/or σ_x and σ_y are very close to zero:

$$C_1 = (K_1L)^2,$$

$$C_2 = (K_2L)^2,$$

$$C_3 = \frac{C_2}{2},$$

where K_1 and K_2 are very small ($\ll 1$) constants and L is the dynamic range of the cell.

Mean squared error (MSE) and peak signal-to-noise ratio (PSNR) were also employed as comparison metrics. The MSE is computed by averaging the squared intensity differences between two cells (Wang and Bovik 2009),

$$MSE = \frac{1}{MN} \sum_{n=1}^N \sum_{m=1}^M [g(n, m) - h(n, m)]^2,$$

where n and m are the x-axis and y-axis cell number in each dataset, $g(n, m)$ and $h(n, m)$, with a total of N and M x-axis and y-axis cells, respectively. MSE is simple to calculate and interpret; the smaller the value, the closer the two datasets match. However, with larger dataset sizes and range in data values, the MSE does not scale well, and becomes difficult to interpret (Wang et al. 2004).

The PSNR avoids the problematic scaling issues of the MSE by adding a scaling term:

$$PSNR = \log_{10} \frac{P}{MSE},$$

where P is the peak value of the image. With the datasets scaled between 0 and 1, a PSNR value of 0

Table 3

Quantitative comparison between datasets using absolute difference (with standard deviation), percent difference (with standard deviation), SSIM, PSNR, and MSE

| Datasets | UAS vs. helicopter | UAS vs. UC ground | UC ground vs. helicopter |
|--------------------------|---------------------|-------------------|--------------------------|
| Mean absolute difference | -16.1 ± 69.8 nT | 0.8 ± 80.2 nT | 16.6 ± 83.7 nT |
| Mean percent difference | $1.9 \pm 3.5\%$ | $2.4 \pm 3.3\%$ | $1.5 \pm 2.1\%$ |
| SSIM | 0.90 | 0.91 | 0.87 |
| MSE | 0.0024 | 0.0034 | 0.0036 |
| PSNR | 26.28 | 24.79 | 24.50 |

implies no similarities between the two datasets and a PSNR of 1 implies the datasets are identical.

As with the absolute difference and percent difference results, the SSIM, MSE, and PSNR, all reveal that the different datasets are nearly indistinguishable from one another (Table 3).

5. Concluding Remarks

5.1. Discussion

This study provided a direct comparison of three magnetic survey datasets—ground, helicopter, and UAS—from a forested area typical of the Canadian Precambrian Shield. Comparison metrics, absolute difference, percent difference, coherence, and structural similarity indices were almost the same for the three datasets taken as a whole. This indicates that the UAS technology is delivering data of the same quality as the traditional ground and helicopter techniques. With autopilot and waypoint navigation, UAS have an additional advantage. They are capable of flying survey lines more tightly spaced than achieved in this study (e.g. 5–10 m line spacing). This opens the possibility of filling niche roles in exploration surveying. UAS are ideal for flying small, very targeted ‘surgical’ surveys, offering quick turn-around of results in the support of near real-time decision making in the field during exploration campaigns. Furthermore, they could have a role in sensitive survey regions, such as: areas populated by people or livestock; environmental protected areas; or regions near international borders.

Geologically complex regions, such as the Druillettes syncline, are examples of locations where lower altitude and tighter line spacing could improve

delineation of geological features. Cunningham et al. (2018) show that it is theoretically possible to distinguish between two structures with a limiting depth of 40 m and a width of 10 m when they are spaced 67.5 m, 45 m, and 22.5 m apart perpendicular to strike at survey altitudes of 100 m, 50 m, and 2 m AGL, respectively. Improved delineation would also be possible with tighter line spacing allowing for the detection of potential discontinuities (e.g., faulting) or structures near-parallel the survey direction. The Geological Survey of Canada recommends a standard altitude to line spacing ratio of 1:2.5 (Coyle et al., 2014); however, this will vary depending on specific client needs and it is common to see a 1:1 ratio (e.g., an altitude of 50 m and line spacing of 50 m). If it were possible to fly a UAS as low as possible, down to a 2 m AGL (vegetation ignored) it would not be unreasonable to design a survey with a 10 m line spacing. Close examination of the RMI maps presented (Figs. 7, 8, 9) revealed subtle differences between the datasets. Features related to IF (Features 1 and 4) are crisply defined in the UAS data, especially near-parallel internal structures that follow the dominant E–W structural trend. The upward continued ground data has also captured these fine details but there remains the issue of not knowing which data has been directly observed versus which data has been generated in interpolation and upward continuation. In contrast to UAS and upward continued ground data, helicopter data is adversely affected by its lower resolution, due to an increased line spacing and higher spatial sampling interval. Notwithstanding economic and safety considerations, the results of this study reinforce the fact that UAS magnetometry has now reached a level of technical

maturity such that it has become a competitive tool in comparison with traditional survey techniques.

5.2. Recommendations for Future Work

Building on the results presented in Cunningham et al. (2018) and this paper, future work could address broader issues in survey design. A study, including both modelling and experimental surveying, could investigate the impact of the following variables on data quality: (1) lateral resolution limits as a function of line spacing; (2) in-line resolution as a function of the sampling interval (changing flight speed or sampling rate); (3) flight altitude and tightness of terrain draping; (4) signal to noise ratio; and (5) economic competitiveness in relation to survey planning, platform endurance, and processing workflows.

Since the UAS platform is an emerging technology, in contrast to the well-established ground and airborne methods, it offers more potential for improvement. In particular, the issue of compensation (Tuck et al., 2019) should be examined carefully. A standard practice of airborne magnetic surveying is the use of aircraft attitude compensation, the removal of in-flight magnetic noise from the changing position and orientation of the aircraft in space. Traditionally, this is performed by flying a high-altitude compensation flight pattern (box or cloverleaf) to remove the effects of local geology, and then by performing a linear least squares analysis to model the aircraft attitude effects. Due to government regulations, in Canada and other countries, UAS are limited to low altitude flying only, so traditional attitude compensation modelling is not an option. Alternative attitude compensation methods need to be developed to quantify and reduce the aeromagnetic noise from aircraft motions during UAS surveying.

Acknowledgements

The authors thank NSERC (Natural Sciences and Engineering Research Council) for providing the Engage grant to Dr. Claire Samson and scholarship to Michael Cunningham.

Funding

Dr. Samson received funding for this research project through the NSERC Engage grant program. Mr. Cunningham received the Canadian Graduate Scholarship (Doctoral) from NSERC.

Declarations

Conflict of interest The authors declare that they have no conflict of interest.

Publisher's Note Springer Nature remains neutral with regard to jurisdictional claims in published maps and institutional affiliations.

REFERENCES

- Bian, J., Wang, X., & Gao, S. (2021). Experimental aeromagnetic survey using a rotary-wing aircraft system: a case study in Heizhugou, Sichuan, China. *Journal of Applied Geophysics*. <https://doi.org/10.1016/j.jappgeo.2020.104245>
- Cherkasov, S., Sterligov, B., & Zolotaya, L. (2016). On the use of unmanned aerial vehicles for high-precision measurements of the Earth's magnetic field. *Moscow University Geological Bulletin*, 71(4), 296–299. <https://doi.org/10.3103/S0145875216040037>
- Coyle, M., Dumont, R., Keating, P., Kiss, F., & Miles, W. (2014). Aeromagnetic surveys: Design, quality assurance, and data dissemination. *Geological Survey of Canada, Open File, 7660*, 48. <https://doi.org/10.4095/295088>
- Cunningham, M., Samson, C., Wood, A., & Cook, I. (2018). Aeromagnetic surveying with a rotary-wing unmanned aircraft system: A case study from a zinc deposit in Nash Creek, New Brunswick, Canada. *Pure and Applied Geophysics*, 175(9), 3145–3158. <https://doi.org/10.1007/s00024-017-1736-2>
- Cunningham, M., Samson, C., Laliberté, J., Goldie, M., Wood, A., & Birkett, D. (2021). Inversion of magnetic data acquired with a rotary-wing unmanned aircraft system for gold exploration. *Pure and Applied Geophysics*, 178, 501–516. <https://doi.org/10.1007/s00024-021-02664-8>
- de Smet, T. S., Nikulin, A., Romanzo, N., Graber, N., Dietrich, C., & Puliaiev, A. (2021). Successful application of drone-based aeromagnetic surveys to locate legacy oil and gas wells in Catteraugus county, New York. *Journal of Applied Geophysics*. <https://doi.org/10.1016/j.jappgeo.2020.104250>
- Funaki, M., Higashino, S., Sakanaka, S., Iwata, N., Nakamura, N., Hirasawa, N., Obara, N., & Kuwabara, M. (2014). Small unmanned aerial vehicles for aeromagnetic surveys and their flights in the South Shetland Islands, Antarctica. *Polar Science*, 8, 342–356. <https://doi.org/10.1016/j.polar.2014.07.001>
- Guha, J., Chown, E. H., & Daigneault, R. (1991). Litho-tectonic framework and associated mineralization of the eastern extremity of the Abitibi Greenstone Belt, Quebec [Field Trip 3]. *Geological Survey of Canada, Open File*. <https://doi.org/10.4095/132276>

- Le Maire, P., Bertrand, L., Munsch, M., Diraison, M., & Géraud, Y. (2020). Aerial magnetic mapping with an unmanned aerial vehicle and a fluxgate magnetometer: A new method for rapid mapping and upscaling from the field to regional scale. *Geophysical Prospecting*, *68*(7), 2307–2319. <https://doi.org/10.1111/1365-2478.12991>
- Lee, M., & Morris, W. (2013). Quality assurance of aeromagnetic data using lineament analysis. *Exploration Geophysics*, *44*, 104–113. <https://doi.org/10.1071/EG12034>
- Malehmir, A., Dynesius, L., Paulusson, K., Paulusson, A., Johansson, H., Bastani, M., Wedmark, M., & Marsden, P. (2017). The potential of rotary-wing UAV-based magnetic surveys for mineral exploration: A case study from central Sweden. *Leading Edge*, *36*(7), 552–557. <https://doi.org/10.1190/tle36070552.1>
- Parshin, A., Morozov, V., Blinov, A., Kosterev, A., & Budyak, A. (2018). Low-altitude geophysical magnetic prospecting based on multicopter UAV as a promising replacement for traditional ground survey. *Geo-Spatial Information Science*, *21*(1), 67–74. <https://doi.org/10.1080/10095020.2017.1420508>
- Parvar, K., Braun, A., Layton-Matthews, D., & Burns, M. (2018). UAV magnetometry for chromite exploration in the Samail ophiolite sequence. *Oman Journal of Unmanned Vehicle Systems*, *6*(1), 57–69. <https://doi.org/10.1139/juvs-2017-0015>
- Sampietro, D., Reguzzoni, M., & Negretti, M. (2013). The GEMMA crustal model: First validation and data distribution. *ESA Special Publications*, *722*, 30.
- Sterligov, B., Cherkasov, S., Kapshtan, D., & Kurmaeva, V. (2018). An experimental aeromagnetic survey using a rubidium vapor magnetometer attached to the rotary-wings unmanned aerial vehicle. *First Break*, *36*(1), 39–45. <https://doi.org/10.3997/1365-2397.2017023>
- Tuck, L., Samson, C., Polowick, C., & Laliberté, J. (2019). Real-time compensation of magnetic data acquired by a single-rotor unmanned aircraft system. *Geophysical Prospecting*, *67*, 1637–1651. <https://doi.org/10.1111/1365-2478.12800>
- Walter, C., Braun, A., & Fotopoulos, G. (2019a). High-resolution unmanned aerial vehicle aeromagnetic surveys for mineral exploration targets. *Geophysical Prospecting*, *68*, 334–349. <https://doi.org/10.1111/1365-2478.12914>
- Walter, C., Braun, A., & Fotopoulos, G. (2019b). Spectral analysis of magnetometer swing in high-resolution UAV-borne aeromagnetic surveys. *IEEE STRATUS*. <https://doi.org/10.1109/STRATUS.2019.8713313>
- Walter, C., Braun, A., & Fotopoulos, G. (2019c). Impact of three-dimensional attitude variations of an unmanned aerial vehicle magnetometry system on magnetic data quality. *Geophysical Prospecting*, *67*, 465–479. <https://doi.org/10.1111/1365-2478.12727>
- Wang, Z., & Bovik, A. C. (2009). Mean squared error: Love it or leave it? *IEEE Signal Processing Magazine*, *26*(1), 98–117. <https://doi.org/10.1109/MSP.2008.930649>
- Wang, Z., Bovik, A. C., Sheikh, H. R., & Simoncelli, E. P. (2004). Image quality assessment: From error visibility to structural similarity. *IEEE Transactions on Image Processing*, *13*(4), 600–612. <https://doi.org/10.1109/TIP.2003.819861>
- Wood, A., Cook, I., Doyle, B., Cunningham, M., & Samson, C. (2016). Experimental aeromagnetic survey using an unmanned air system. *The Leading Edge*, *35*, 270–273. <https://doi.org/10.1190/tle35030270.1>
- Carrier A, Nadeau-Benoit V, Faure S (2019) NI 43-101 Technical Report and Initial Mineral Resource Estimate for the Nelligan Project, Quebec, Canada. Accessed 08 Jan 2020, https://vanstarmining.com/wp-content/uploads/2019/12/IAMGOLD_VANSTAR_43-101_FINAL.pdf
- Eck, C., & Imbach, B. (2011). Aerial magnetic sensing with an UAV helicopter. In *International archives of photogrammetry, remote sensing, and spatial information sciences*. Volume XXXVIII-1/C22. ISPRS Zurich 2011 Workshop. 10.5194/isprsarchives-XXXVIII-1-C22-81-2011
- Government of Canada. (2017). Geospatial data extraction. Accessed 18 Aug 2020. <https://maps.canada.ca/czs/index-en.html>
- SIGEOM. (2020). Système d'information géominière du Québec. Accessed 15 July 2020, <http://sigeom.mines.gouv.qc.ca/>
- Stoll, J. (2013). Unmanned aircraft systems for rapid near surface geophysical measurements. The International Archives of the Photogrammetry, Remote Sensing and Spatial Information Sciences. <https://doi.org/10.5194/isprsarchives-XL-1-W2-391-2013>
- Zhang, B., Guo, Z., & Qiao, Y. (2011). A simplified aeromagnetic compensation model for low magnetism UAV platform. In *IEEE international symposium, IGARSS*. <https://doi.org/10.1109/IGARSS.2011.6049950>

(Received August 26, 2021, revised March 5, 2022, accepted April 2, 2022, Published online April 27, 2022)